Clinical Neurophysiology 130 (2019) 1926–1936

Contents lists available at ScienceDirect

Clinical Neurophysiology

journal homepage: www.elsevier.com/locate/clinph

A new potential specifically marks the sensory thalamus in anaesthetised patients

Jesús Pastor *, Lorena Vega-Zelaya

Clinical Neurophysiology and Fundación de Investigación La Princesa, Hospital Universitario La Princesa, Madrid, Spain

ARTICLE INFO

Article history:
Accepted 16 July 2019
Available online 8 August 2019

Keywords:
Centromedian
Deep brain stimulation
High frequency oscillations
Microelectrode recordings
Somatosensory evoked potentials
Ventral caudal

HIGHLIGHTS

- Very high frequency oscillations in the thalamus are not produced in the ventral caudate nucleus only.
- High frequency oscillations in the ventral caudate nucleus reflect the synapses of thalamic neurons.
- High frequency oscillations can be a specific landmark for sensory thalamus in anaesthetized patients.

ABSTRACT

Objective: During deep brain stimulation (DBS) surgery, we analysed somatosensory evoked potentials (SSEPs) using microelectrode recordings (MERs) in patients under general anaesthesia.
Methods: We obtained MERs from 5 patients with refractory epilepsy. Off-line analysis isolated local field potentials (LFPs, 2–200 Hz) and high frequency components (HFCs, 0.5–5 kHz). Trajectories were reconstructed off-line.
Results: The ventral caudate (V.c.) nucleus was most frequently recorded from (171 mm). Very high frequency oscillations (VHFOs) were recorded up to 8 mm in length from all 4 electrodes but were most frequently recorded from the V.c. The properties of VHFOs were similar among all nuclei (frequency >1500 Hz, amplitude ~3 μV, starting time ~14 ms, duration 8–9 ms). Consecutive recordings did not show any synchronization or propagation, but a new kind of potential (high frequency oscillation, HFO) appeared abruptly inside the V.c. (frequency = 848 ± 66 Hz, amplitude = 5.2 ± 1.8 μV starting at 17.7 ± 0.5 ms, spanning 3.4 ± 0.3 ms).
Conclusions: VHFOs are widely extending and cannot be ascribed to the V.c. HFOs in patients under general anaesthesia can serve as a landmark to identify the V.c. in thalamic DBS surgery.
Significance: Thalamic processing involves nuclei other than the V.c, and HFO can be used to improve DBS surgery.

1. Introduction

The human thalamus is a complex egg-shaped structure composed of more than 50 different sub-nuclei (Nieuwenhuys et al., 2008). Deep brain stimulation (DBS) is used to target some of these sub-nuclei, such as the centromedian nucleus (Ce) for the treatment of drug-resistant epilepsy, pain or Gilles de la Tourette syndrome (Owen et al., 2006; Shields et al., 2008; Valentín et al., 2013). This nucleus is partially surrounded by the anterior medial portion of the ventral caudate nucleus (V.c.); at some angles, a trajectory through the V.c. can be used to gain access to the Ce. DBS in the V.c. provides the opportunity to record somatosensory evoked potentials (SSEPs) from final DBS electrodes (Katayama and Tsubokawa, 1987; Hanajima et al, 2004a;) and microelectrode recordings (MERs) (Hanajima et al., 2004a). The V.c. response to electrical stimulation comprises two components (Klostermann et al., 2000; Klostermann et al., 2002; Hanajima et al., 2004a): a

Abbreviations: Ce, centromedian nucleus; DBS, deep brain stimulation; DDNN, dorsal nuclei; CWT, continuous wavelet transform; FFT, fast Fourier transform; HFC, high frequency component; HFO, high frequency oscillation, LFP, local field potential; MERs, microelectrode recordings; MRI, magnetic resonance imaging; SSEP, somatosensory evoked potentials; SW, Schaltenbrand-Wahren; V.c., ventral caudate nucleus; VHFO, very high frequency oscillation; V.im., ventrointermedial nucleus; V.o., ventral oralis nucleus.

* Corresponding author at: Neurofisiología Clínica, Hospital Universitario de La Princesa, C/Diego de León 62, Madrid 28006, Spain. Fax: +34 91 4013582.
E-mail address: jesus.pastor@salud.madrid.org (J. Pastor).

https://doi.org/10.1016/j.clinph.2019.07.026
1388-2457/

local field potential (LFP) and a very high frequency oscillation (VHFO) of approximately 1–1.5 kHz. VHFOs are most likely generated by thalamo-cortical projection neurons (Klostermann et al., 2002; Hanajima et al., 2004a) and may serve as a landmark for the V.c. nucleus (Yamashiro et al., 1989; Shima et al., 1991; Hanajima et al., 2004b; Yeh et al. 2010). In this work, we defined VHFOs as all potentials with a mean frequency above 1.2 kHz and high frequency oscillations (HFOs) as potentials with a mean frequency below 1.2 kHz (Usui et al., 2010).

In awake patients, the V.c. is customarily identified by response to light touch (Obwegeser et al., 2000) or the presence of paraesthesia from electrical stimulation (Wu et al., 2014). However, in anaesthetized patients, conscious collaboration is precluded. Therefore, finding landmarks that positively identify some definite thalamic nuclei is extremely important. For this purpose, one of the most obvious possibilities would be using SSEP to identify the V.c.

The aim of our study was to analyse the neural response to somatosensory stimuli obtained using MERs in patients under general anaesthesia while undergoing a DBS operation at the Ce for pharmacoresistant epilepsy. Considering the relative position between the Ce (the target) and V.c., we used the passage through the last nucleus to study SSEP and identify the Ce in a positive manner. We observed a new response (Vega-Zelaya et al., 2016a), termed HFO, that has not been previously described and realized that thalamic processing of SSEPs from the superior member implies the participation of other nuclei in addition to the V.c. The properties of this response were not well established in our preliminary report. Therefore, in this manuscript, we have addressed this goal in a different group of patients.

Preliminary results were published as an abstract (Vega-Zelaya et al, 2017).

2. Methods

For this work, we followed the Schaltenbrand-Wahren (SW) atlas (Hassler, 1959) nomenclature. The parafascicullaris/centrome dian (Pf/CM) mentioned in the literature (Peppe et al., 2008; Semenova et al., 2016) is the Ce, and the ventro-posterolateral and ventro-posteromedial (VPL/VML) nuclei are equivalent to the V.c. (Owen et al., 2006; Nguyen et al., 2011).

2.1. Patients

We studied 5 patients undergoing surgery for chronic DBS treatment in the Ce. All patients gave free and informed consent to the procedures approved by the Hospital La Princesa Ethics Board.

Patients were initially assessed for study suitability using a presurgical evaluation in our centre (Pastor et al., 2005; Sola et al., 2005) and excluded from resective surgery. Most patients were treated using vagus nerve stimulation (VNS), but after a two-year period of inadequate results, DBS in the Ce nucleus was proposed.

2.2. Surgical procedures

All patients were operated on while under general anaesthesia using propofol (5.48 ± 0.28 mg/kg/h, [4.5, 6.2]) and remifentanil (0.12 ± 0.02 μg/kg/min, [0.1, 0.2]), maintaining a bispectral index (BIS) between 40 and 45. Neuromuscular blockade was accomplished with cis-atracurium (0.5 mg/kg).

The thalamus was identified using 1.5 T magnetic resonance imaging (MRI; General Electric®, Fairfield, CT, USA), and coordinates were located stereotactically with a neuronavigator (BrainLab®, Feldkirchen, Germany). Coordinates were calculated by fusing the MRI image and CT scan according to the SW atlas. For thalamic DBS electrode placement, a tentative initial target was selected in the Ce (x = 8, y = −10, z = 0). All coordinates refer to the mid-intercommissural anterior commissure-posterior commissure (AC-PC) line. Neuronal recordings (Leadpoint®, Minneapolis, USA) were obtained beginning 10 mm above the target and progressing in steps of 0.5 mm. Microelectrode recordings (MERs, FHC®, Maine, USA) were obtained from both spontaneous and sensory-evoked activity until the inferior border of the thalamus was confirmed by the absence of neuronal activity. The impedance was always above 900 kΩ (1696 ± 80 kΩ, [900, 2900]).

MERs were obtained through four microelectrodes separated by 2 mm and placed (usually) at anterior, centre, posterior and lateral locations except in patient 5 in whom posterior electrodes were replaced by medial electrodes. A microdrive was fixed to a stereotactic Leksell Coordinate Frame (Elekta®, Stockholm, Sweden). The bandwidth for spontaneous activity was 200–5 kHz except for SSEPs for which it was 2–5 kHz, with a sample rate of 24 kHz in both cases. The notch filter was off. However, in two trajectories, recordings were performed with the notch filter on. For SSEPs, the notch filter was used in only one patient.

After the Ce was identified, a quadripolar DBS electrode was implanted. During the same surgery, the leads were connected to an implanted programmable stimulator placed in a pectoral or abdominal location.

2.3. Somatosensory evoked potentials

SSEP recordings were started at 8 mm above the theoretical target and repeated at 1 mm intervals until the end of the thalamus. At every point, two rounds of 500 pulses were delivered. Stimulation was elicited by electrical stimulation of the contralateral median nerve at the wrist by means of surface electrodes (Ambu®, Baltorpbakken, Denmark), with an intensity 1.5 times higher than the motor threshold (usually approximately 20 mA) and 200 μs pulses at a frequency of 7.1 Hz (Vega-Zelaya and Pastor, 2015; Vega-Zelaya et al., 2016a). In some patients, stimulation at the ipsilateral median nerve or sham stimulation at 0 mA was also performed. Responses at the cervical point (C2-Fpz) and both parietal regions (C3′/C4′-Fpz) were recorded by 18 mm subdermal needles (SGM®, Ljubiceva, Croatia) with a bandwidth of 10–1500 Hz, with the notch filter off. Scalp recordings were performed only as a demonstration that electrical stimulation was effective. Therefore, we were not interested in the properties of those potentials, and consequently, we have not analysed them. Simultaneously, the activity recorded through the four microelectrodes was averaged across trials (Fig. 1A).

2.4. Reconstruction of the trajectory

To identify all the sub-nuclei included in the trajectory of each microelectrode, we reconstructed the real trajectories and projected them onto an SW map of neuroanatomy. To accomplish this goal, we considered the real x_r and y_r coordinates measured by MRI (Appendix A, Table A.1) performed one month after surgery and represented (scaled according to AC-PC distance) them on the last axial plane of the SW map, including the floor of the thalamus (z = 0). We defined this point as the real end-point $\vec{r}_{ep} = (x_r, y_r, 0)$. Usually, during DBS surgery, real brain coordinates are disparate from theoretical ones calculated by neuronavigation, especially for the z-axis. This inconsistency is due to the drainage of cerebro-spinal fluid or air entry. To avoid this problem and to be certain regarding the relationship between the recordings and the thalamus, we considered z = 0 the last recording inside the thalamus defined by the presence of action potentials, irrespective of the z-theoretical coordinate computed during MER. All z coordi-

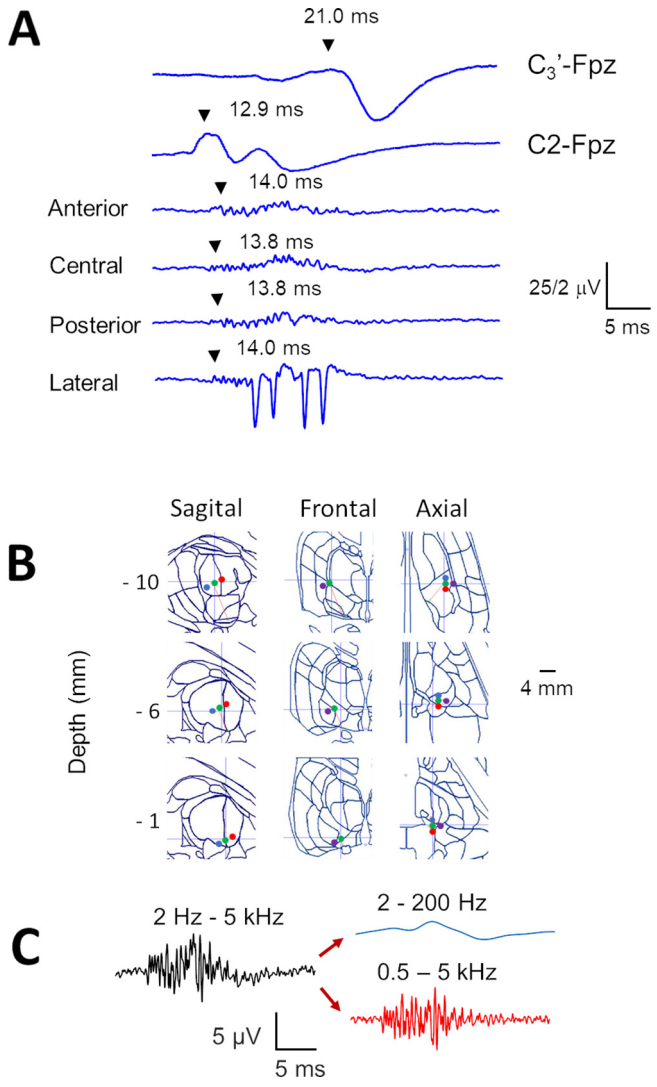

Fig. 1. Methods and reconstruction. (A) SSEPs recorded from the cervical point, scalp and microelectrodes. Relevant times are shown. (B) Reconstruction of the trajectory from one patient, showing microelectrode (anterior = blue, central = green, posterior = red and lateral = purple) positions at different depths superimposed onto an SW map. (C) A raw trace (black) acquired with the indicated bandwidth and off-line processing of LFPs (blue) and HFCs (red) acquired at different bandwidths.

nates for the recordings were defined and corrected when needed according to this criterion.

The angles used during the MER trajectory (ring and arch) were the same as those measured from the final DBS electrode during the post-op MRI. Starting from $\vec{r}_{ep}$ and considering the angles, we were able to reconstruct the real trajectory of the electrode in a three-dimensional space in 1 mm intervals (Appendix B). To select the nearest SW plane, we used only the trajectory corresponding to the centre electrode, which was the same electrode considered during the planning process. However, we reconstructed trajectories for all four electrodes. Frontal (F), sagittal (S) and axial (A) planes of the SW atlas were digitized in individual jpg files, and every file was identified by the distance to intercommissural midpoint (i.e., S035 for the sagittal SW plane located at 3.5 mm to midpoint, Fa035 for the SW plane located 3.5 mm anterior to the midpoint or Ad035 for the SW plane located 3.5 mm above the midpoint). For every dimension, SW is a set of irregular and discrete series of planes (20 for the frontal, from Fa165 to Fp155, 20 for the axial, from Av085 to Ad160 and 17 for the sagittal, from S015 to S275). For every distance to $\vec{r}_{ep}$, the coordinates where the central electrode was placed could be easily identified (x_{ce}, y_{ce}, z_{ce}). Then, we obtained the orthogonal planes, including this point, and for every plane, we selected the closest plane from the series of jpg files. This algorithm was implemented in a MATLAB® R2016 script (MATLAB, Natick, USA). For every plane, we plotted the projection of the four microelectrodes. Therefore, we were able to identify where the nucleus corresponding to each electrode was located throughout a trajectory using the SW map (Fig. 1B).

The probability of passing through a nucleus was defined as the ratio between total length (in mm) recorded for that nucleus and the total length (in mm) recorded for every electrode. In both cases, the contribution of all patients was considered. For example, if we recorded this set of lengths for the nucleus n as $\{l_1^n, l_2^n, \cdots l_5^n\}$ where n = Ce, ventrointermedial (V.im), V.c., etc., and we recorded this set of lengths through electrode k $\{l_1^k, l_2^k, \cdots l_5^k\}$ where k = anterior, central, etc., then, the probability of recording the nucleus n by electrode k is

$$p(n/k) = \sum_{i=1}^{5} \frac{l_i^n}{l_i^k}$$

To calculate the error between electrode positions obtained by reconstruction and electrode position in SW planes, we computed the orthogonal projection from the trajectory point to the sagittal, frontal and axial planes.

To avoid bias, we performed identification of nuclei during reconstruction blindly in the presence of potentials from every electrode.

2.5. Analysis of SSEP

Data were exported to ASCII files, and analyses were performed off-line. Recordings spanned 100 ms (2400 points). To avoid capacitive artefacts, we discarded the first 10 ms.

We tried three different digital filters for analysis, e.g., Butterworth, Bessel and Chebyshev. However, as the results were similar in all cases, the analysis was performed using a 6th order Butterworth filter (Van Drongelen, 2007a). Raw recordings were digitally filtered at two different bandwidths: i) a low bandwidth from 2-200 Hz and ii) a high bandwidth from 500 Hz-5 kHz. The first bandwidth was used to identify LFPs (Rey et al., 2015), and the second was intended to isolate higher frequency oscillations (Fig. 1C). This element was termed the high frequency component (HFC; Kato et al., 2003). To avoid undesired effects due to filtering, we used zero-phase forward and reverse digital IIR filtering.

To avoid bias due to subjective threshold identification, we achieved automated detection for significant points by defining the upper and lower thresholds for LFP and HFC recordings. Both thresholds were defined as $\bar{V} \pm 2.5\sigma_V$ where $\bar{V}$ is the mean value of the first 60 points (2.5 ms), and σ_V is the standard error.

The phases of LFPs were defined as voltage values significantly different from the threshold that returned to the basal level. These values were designated according to the neurophysiological criterion as N if negative (upward deflection) or P if positive (downward deflection) and the ordinal value of their appearance. For every phase, the maximum amplitude and latency at that point were computed.

For HFC, we determined the amplitudes, latencies and polarities of peaks, defined as a voltage exceeding the threshold. Intervals between consecutive peaks were used to compute instantaneous frequency. The time-frequency structure of the HFCs was assessed by means of wavelet analysis. For visualization, a discretized

continuous wavelet transform was applied to the data with a symlet wavelet as the mother wavelet (continuous wavelet transform, CWT; Van Drongelen, 2007b).

For both LFPs and HFCs, the main frequency components were identified by using a periodogram of the whole recording with the fast Fourier transform (FFT). In the case of HFCs, components were sub-divided into HFOs or VHFOs according to whether they were lower or higher than 1.2 kHz, respectively. We selected 1.2 kHz instead of the most common 1 kHz because periodograms showed a clear notch around this frequency.

To compute the relative contribution of low and high frequencies, we normalized all spectra to the high components over 1.2 kHz and then computed the mean spectra for every nucleus. Areas for low (between 500–1200 Hz) and high frequencies (1200–5000 Hz) as well as a low/high ratio were calculated.

Synchronization between pairs of HFC recordings was computed using Pearson's correlation coefficient (ρ_{ij}- Ortega et al. (2008)) and cross-correlation (Vega-Zelaya et al., 2016b) at 100 and 500 μs lags ($C_{ij}(100)$, $Cij(500)$, see Appendix C). We selected a time window between 13 and 26 ms (spanning all periods occupied by VHFCs) to compute synchronization. The entire record for every patient can be considered a $k \times 4$ matrix (see Fig. 2A) where k = 6–10. We grouped the traces in two ways: (i) recordings at the same depth, x_i, i = 1, 2, 3, 4; and (ii) recordings pertaining to the same nucleus that were defined according to the trajectory reconstructed, y_i, i = 1, 2…N. Therefore, for every pair of HFO traces (x_i,x_j) from either the same depth or the same nucleus, we computed ρ_{ij} and $C_{ij}(100)$, $Cij(500)$. Then, we obtained the mean value ($\bar{\rho}_{ij}$) and mean standard error ($SEM\rho_{ij}$) according to these formulas:

$$\bar{\rho}_{ij} = \frac{1}{k}\sum_{i,j=1;i\neq j}^{k} \rho_{ij} \quad SEM\rho_{ij} = \sqrt{\frac{\sum_{i,j=1;i\neq j}^{k} (\rho_{ij} - \bar{\rho}_{ij})^2}{k-1}}$$

and the mean value ($\bar{C}_{ij,\tau}, \bar{\rho}_{ij}$) and mean standard error ($SEM_{C_{ij,\tau}}$SEMρ_{ij}) for cross-correlation at different times, following these formulas

$$\bar{C}_{ij,\tau} = \frac{1}{k}\sum_{i,j=1;i\neq j}^{k} C_{ij,\tau} \quad SEM_{C_{ij,\tau}} = \sqrt{\frac{\sum_{i,j=1;i\neq j}^{k} (C_{ij,\tau} - \bar{C}_{ij,\tau})^2}{k-1}}$$

where k = 1, 2…4 for synchronization at the same depth and k = 1, 2…N for different nuclei.

All analyses were performed with custom-made MATLAB®R2016 scripts.

2.6. Statistics

Statistical comparisons between groups were performed using the z-score, Student's t-test for data with normal distributions or the Mann-Whitney rank sum test for non-normal distributions. Normality was evaluated using the Kolmogorov-Smirnov test. SigmaStat 3.5 software (Point Richmond, USA) was used for statistical analysis. Instead of using rank as a dispersion measure, we used a 25–75 interpercentile range that is shown between brackets.

The significance level was set at p = 0.05. The results are shown as the mean ± SEM, except where indicated otherwise.

3. Results

3.1. Reconstruction of trajectories

We reconstructed trajectories from 5 patients (3 men, 2 women, Table 1) who underwent general anaesthesia. At each step, we plotted the reconstructed coordinate for all electrodes onto the closest SW plane; therefore, we identified the thalamic nucleus from which recordings originated (Fig. 2A and see Fig. 1B). The mean error originating from the discrepancy between the position in the trajectory and the closest SW plane was slightly lower than 1 mm (see Appendix A, Table A.2 and Supplementary Fig. A).

Along the trajectories, we focused on the following nuclei: the Ce, V.c., V.im., ventral oralis (V.o.), and collective dorsal nuclei (DDNN, e.g., dorsalis-intermedius or ventro-intermedius). The total length of the trajectories through these nuclei (summed across all electrodes and subjects) measured 171 mm in the V.c., 99 mm in the Ce, 83 mm in the V.im., 15 mm in the V.o. and 72 mm in the DDNN.

The probability of passing through a nucleus of interest, which was computed as the ratio between the length recorded for a

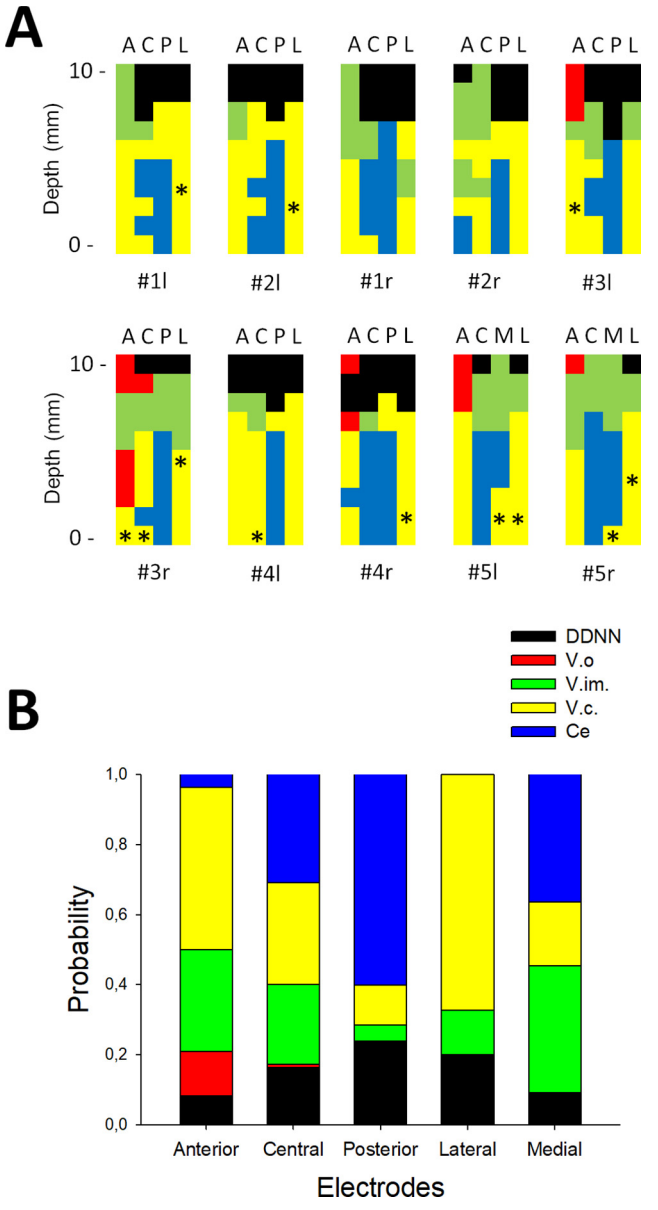

Fig. 2. Trajectories. (A) Trajectories of the electrodes (A = anterior, C = central, P = posterior, L = lateral, M = medial) showing the recorded nuclei in different colours. Black = DDNN; red = V.o.; green = V.im.; yellow = V.c.; blue = Ce. Asterisks indicate the presence of HFOs. (B) Differential probability of recording thalamic nuclei from different electrodes.

Table 1
Clinical features of patients studied.

Patient	Gender	Age (years)	History (years)	Etiology	MR	v-EEG	VNS
#1	F	37	31	Genetic*	Normal	GE	Yes
#2	M	34	27	Genetic**	Normal	GE/EE	Yes
#3	F	18	12	LGS	Dysplasia LF	GE	No
#4	M	30	23	Structural	Dysplasia biFT	GE/EE	Yes
#5	M	27	27	LGS	Normal	GE	No

F: female. M: male. EE: epileptic encephalopathy. GE: generalized epilepsy. LF: left frontal. biFT: bilateral fronto temporal. LGS: Lennox-Gastaut syndrome. *20 ring-chromosome syndrome. **Tuberous sclerosis.

definite nucleus and the total length (defined as the sum of all the trajectories performed for every electrode), was different for each of the four electrodes (Fig. 2B). The probability of passing through the Ce was greater for the posterior electrode (0.602), while passing through the V.c. was greater for the lateral electrode (0.673).

3.2. Local field potentials and very high frequency oscillations

At every depth, LFPs and VHFOs were isolated using different filter bandwidths, as stated above. Both potentials have been previously described but using different electrodes, therefore obtaining different results.

Different degrees of complexity were observed in LFPs, although two phases were usually observed (Fig. 3A). These potentials were obtained in 184 occasions, although when obtained isolated, they were extremely small and practically residual (lower than 1 μV). In fact, most of the recordings (172/184) started with an N1 phase, which has an amplitude of 2.3 ± 0.1 [1.1–2.7] μV and a latency of 19.4 ± 0.2 [18.9–20.4] ms. In the remaining recordings (12/184), the first potential was P1, with an amplitude of −2.1 ± 0.2 [−2.3 to −1.0] μV and a latency of 18.4 ± 0.4 [15.9–20.9] ms.

VHFOs were the second most frequent component and were observed on 176 occasions. VHFOs appeared alongside long trajectories (up to 8 mm) and frequently in all four electrodes. Reconstruction of trajectories allowed us to identify the presence of these potentials in different nuclei (Fig. 3A). We obtained 89 VHFOs from the V.c., 17 from the V.im., 65 from the Ce, 3 from the DDNN and 2 from the V.o. The probability of obtaining VHFOs from each of these nuclei was 0.520, 0.205, 0.657, 0.042 and 0.133, respectively. The V.c. and Ce participated in more than 50% of the SSEPs recorded. Interestingly, the probability of obtaining VHFOs was higher for the Ce nucleus than for the V.c. However, these responses were highly specific and associated to somatosensory stimuli because responses completely vanished when the ipsilateral median nerve was stimulated (Fig. 3B). In the same way, sham stimulation with 0 mA did not elicit any response. To determine whether VHFOs depended on the nuclei from which they were recorded, we analysed several properties. The features of VHFOs were similar in all nuclei (Table 2). We also addressed the temporal relationship between LFPs and VHFOs. VHFOs always preceded LFPs by 2.7 ± 0.3 [1.8–3.3] ms (Fig. 3C). However, the relationship between the last part of LFPs and VHFOs was more elusive. LFPs were quite similar to raw recordings (Supplementary Fig. B), and no significant modifications were observed by the effect of filtering; also in these cases, VHFOs preceded LFPs.

The CWT for VHFOs showed two distinct portions. The first portion included lower components between 300–1500 Hz and higher components up to 3500 Hz and coincided with the first portion of the LFPs. The second occurred during the positive portion of the LFP wave and showed lower frequencies (300–1500 Hz, Fig. 3D). Finally, we addressed the potential synchronization between VHFOs (Hashimoto, 2000; Hanajima et al. 2004a). Neither changes in the mean synchronization nor propagation (cross-correlation at τ = 100, 500 μs) were observed at different depths (Fig. 3E, left column). Comparing the mean synchronization for the nuclei Ce, V.c. and V.im also did not reveal any difference in mean values or propagation (Fig. 3E, right column).

3.3. High frequency oscillations

In addition to LFPs and VHFOs, we found a new kind of potential associated with SSEPs that has not been previously described in detail. We defined HFOs as responses generated by SSEP that had higher amplitudes than VHFOs and a mean frequency that did not exceed 1.2 kHz (Fig. 4).

HFOs began at 17.7 ± 0.5 ms [16.1–18.9 ms], ended at 21.1 ± 0.5 ms [19.5–22.9 ms], and spanned 3.4 ± 0.3 ms [2.5–4.2 ms]. Therefore, HFOs always appeared inside the period where VHFOs were present (Fig. 5A). The mean frequency was 848 ± 66 Hz [700–865 Hz], while the maximum voltage was 5.2 ± 1.8 μV [3.7–7.9 μV], which was always positive. In the same places where HFOs were recorded, spontaneous action potentials were mostly negative (Appendix D and Supplementary Fig. C).

The presence of HFOs modified the previous consecutive waveforms of LFPs (Fig. 5A). HFOs were observed in the recordings of the V.c. nucleus only (see Fig. 4, 5B and asterisks in Fig. 2A) and were never recorded from more than one consecutive point.

The time-frequency structure was completely distinct between HFOs and VHFOs as observed from CWT because the amplitudes of the wavelet-transformed HFOs were 10 times greater than those of VHFOs. Additionally, the main components of the structure were clearly under 1.2 kHz, although faster components were also observed (Fig. 5C).

A comparison of normalized areas of power spectra showed that components under 1.2 kHz were clearly dominant in HFOs, and this signature also dominated in the V.im., while higher frequencies were observed in the V.c. and Ce (Fig. 5D). Additionally, the ratio of low/high frequencies was greater for HFOs in the V.c, differing from those in the Ce and V.c. but not from those in the V.im., most likely due to the greater number of low frequencies observed in this nucleus (Fig. 5E). However, excluding some bias in the trajectory reconstruction due to inaccuracy from the discrete SW planes is not possible. Considering that the V.im nucleus is less commonly recorded, a small number of inaccuracies in the reconstruction of this nucleus would have greater effects than those in the reconstruction of other nuclei. However, other possibilities cannot be excluded and remain to be elucidated.

4. Discussion

First, from a methodological consideration, remembering that all patients were under general anaesthesia is important. General anaesthesia can modify neuronal discharge features and perhaps the synaptic functions of some thalamic nuclei (Sloan, 2002; Hutchison, 2004; Voss et al., 2008), although the exact degree remains to be elucidated. However, the main features of scalp SSEP

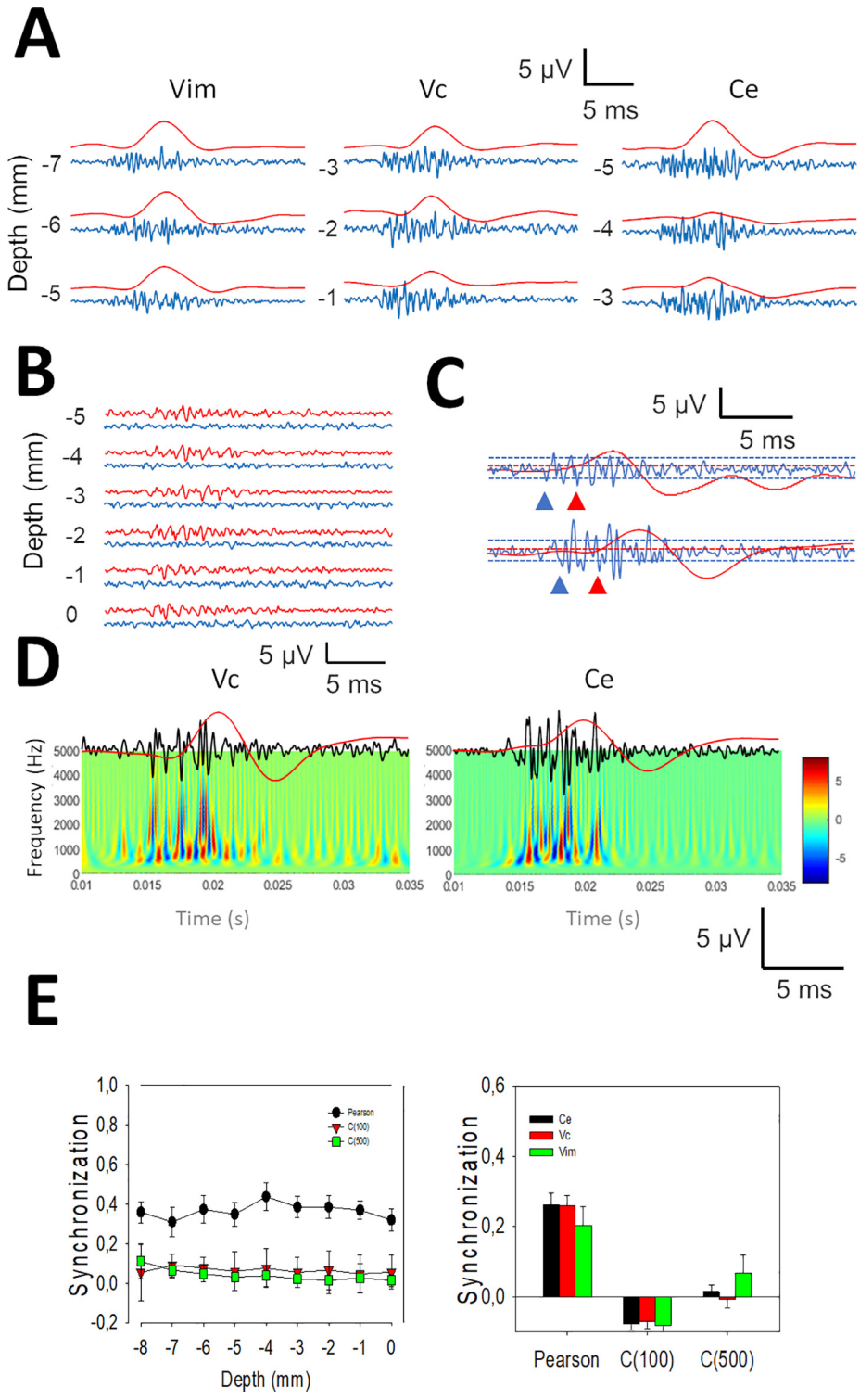

Fig. 3. Properties of LFPs and VHFOs. (A) VHFOs (blue) and LFPs (red) recorded from the V.im., V.c. and Ce nuclei at several depths. (B) VHFOs induced at different depths after stimulation of the contralateral median nerve (red). Absence of response when the ipsilateral median nerve is stimulated (blue). (C) VHFOs (blue) always precede LFPs (red) in the V.c. (upper row) and Ce (lower row). Coloured arrowheads indicate the beginning of each type of oscillation. Dashed lines represent the threshold for LFPs (red) and VHFOs (blue). (D) Time-frequency structure of HFOs from the V.c. (left) and Ce (right) obtained by CWT. (E) Left: mean synchronization (solid dots) and cross-correlation at two different lags (red triangles for C (100) and green squares for C (500)) for all the depths (x-axis) recorded. Right: Mean synchronization and cross-correlation (lags = 100 and 500 μs) for several nuclei. Black = Ce; red = V.c.; green = V.im.

in awake and anaesthetized patients are similar, allowing intraoperative monitoring under general anaesthesia (Vega-Zelaya et al., 2016c), although amplitudes and latencies in SSEP during intraoperative neurophysiological monitoring and awake patients could be slightly different (Møller, 2011). Therefore, we do not expect that the main properties of potentials recorded in anaesthetized

Table 2
Properties of VHFOs for different nuclei. No statistically significant differences have been observed (One-way ANOVA test).

Nucleus	N	Start (ms)	End (ms)	Duration (ms)	Frequency (Hz)	Amplitude (μV)
V.c	77	14.5 ± 0.1	22.6 ± 0.3	8.1 ± 0.3	1659 ± 57	2.8 ± 0.2
V.im.	17	14.5 ± 0.2	23.8 ± 0.6	9.3 ± 0.7	1786 ± 108	3.1 ± 0.4
Ce	65	14.7 ± 0.1	23.4 ± 0.2	8.7 ± 0.2	1718 ± 68	2.9 ± 0.3
DDNN	3	13.6 ± 0.1	22.9 ± 1.2	9.4 ± 1.2	2292 ± 90	3.2 ± 0.4

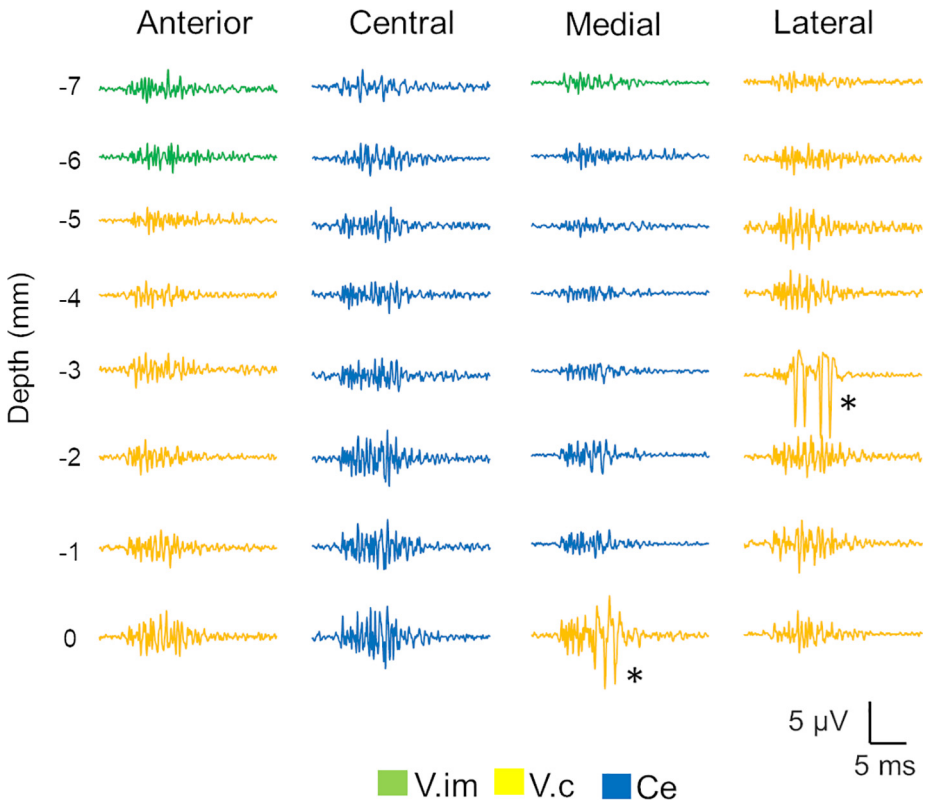

Fig. 4. Example of a long-range recording for all four microelectrodes (indicated above). VHFOs are shown at all points; however, HFOs appear at only two places (−3 and 0 mm) in lateral and medial electrodes, as indicated by asterisks. Thalamic nuclei identified by the reconstruction are indicated in different colours.

patients could be qualitatively different from those obtained in awake patients, although we expect that some variables can quantitatively change in awake patients. The exact degree of dissimilarity can be ascertained by comparing results with those obtained from awake patients during DBS surgery that require conscious collaboration (e.g., V.c. stimulation to treat pain or V.im. stimulation to treat tremor).

Another relevant methodological issue is the reconstruction of trajectories. In a complex structure such as the thalamus, a placement a couple millimetres away can involve a completely different nucleus. Hence, obtaining knowledge of the position where the electrode is placed as accurately as possible is extremely important. During DBS surgery, drainage of cerebro-spinal fluid or air entry inside the cranium can displace the target as much as several millimetres from its theoretical coordinates (Brahimaj et al., 2018; Chen et al., 2018). To avoid this problem, we used an anatomical landmark as well as the absence of neuronal action potentials; in this way, we defined the inferior limit of the thalamus. In addition, real antero-lateral coordinates have been obtained from post-op MRI, which also allowed us to confirm the angles. Therefore, reconstruction of the real trajectory is possible using the formulas given in Appendix B, and these trajectories (each for every electrode) can be straightforwardly plotted in the SW planes. The SW plane is a discontinuous spatial irregular series of planes, and the reconstructed trajectory is also a regularly spaced spatial series (1 mm interval). Therefore, it is easily understandable why both series did not coincide at every point. We have solved this problem by approaching the SW plane closer to the reconstructed point, but this imprecision can be approximately 1 mm in the worst case, although it was usually lower.

LFP and VHFO have been previously described but generally using macroelectrodes (Yamashiro et al., 1989; Shima et al., 1991; Hanajima et al., 2004a; Yeh et al., 2010), and the only studies with semi-microelectrodes (Hanajima et al., 2004b) reported impedances between 100–500 KΩ, approximately one-fourth of our impedance values. The results obtained for those studies are only partially superimposable to ours. Potentially, LFPs could be generated by the positive field originating from excitatory post-synaptic potentials from V.c neurons. However, these potentials had a shorter latency, and the amplitude was more than 10 times higher than our amplitudes. These discrepancies can be explained by the different electrode size and the state of the patients, who

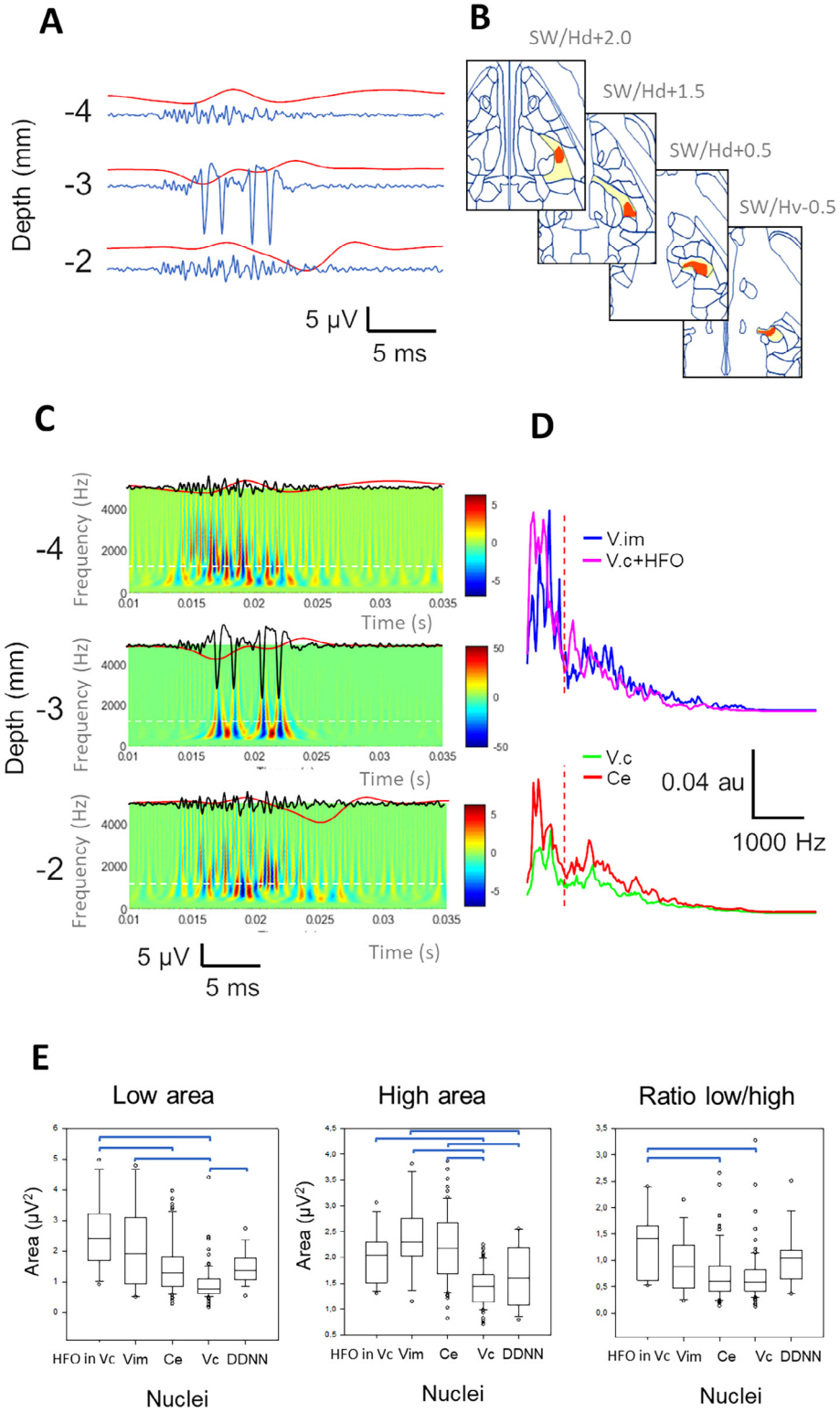

Fig. 5. Properties of HFOs. (A) Well-defined HFOs (middle blue trace) flanked above and below by VHFOs (top and bottom blue traces). The LFPs (red traces) are distorted in the presence of HFOs. (B) Sagittal plates of the SW map showing the areas where HFOs were recorded (red). The V.c. nucleus is highlighted in yellow (C) Comparison of the time-frequency structure for VHFOs and HFOs. White dashed lines indicate a frequency of 1.2 kHz. Please note the different scales. (D) Mean normalized spectra for V.im. (blue) and V.c. + HFOs (pink) are shown in the upper row, and V.c. (green) and Ce (red) are shown in the lower row. Vertical dashed lines indicate 1.2 kHz. (E) Box plots of the mean area of different nuclei exhibiting high frequencies (left column), high frequencies (middle) and the low/high ratio. Horizontal bars indicate $p < 0.05$ (Mann-Whitney test).

were awake in the previous studies. We have generally observed LFPs associated with VHFOs. VHFOs preceded the development of LFPs by more than 2 ms. Therefore, we propose that VHFOs are, in fact, the sources of LFPs created by extracellular currents injected from neuronal structures showing VHFOs into the extracellular space. Nevertheless, we recognize that alternative

explanations could be rose, even it can be discussed the threshold method used to define the latency. HFOs, which are probably generated by sources different from VHFOs, change the morphology of LFPs. However, our results were acquired through high impedance MER, and it can be argued that we mainly recorded multi-unit activity, which is probably different from LFPs recorded through macroelectrodes. Therefore, we cannot conclude that both kinds of recordings, although phenomenologically similar, correspond to the same generators.

The most detailed descriptions of the analysis of VHFOs were made with macroelectrodes (Morioka et al., 1989; Hanajima et al., 2004a, 2004b; Klostermann et al., 2002, Shima et al., 1991). The characteristics described are similar to those in our study in terms of latency and frequency (1408 ± 170 Hz) and less for duration and amplitude, which were approximately one-tenth of those in our study. Some authors compared the features of the VHFOs between the definitive electrode and MER (Hanajima et al., 2004a; Shima et al., 1991), concluding that synchronization is similar. Nevertheless, as stated above, at least some differences can be explained by the collective effect of greater volumes of tissue recorded through macroelectrodes, while all or most of our potentials are local effects. This finding can explain why we have not observed significant synchronization or propagation along the thalamus.

Some publications associate the presence of VHFOs with the sensory thalamus and other sensory areas (Canedo et al., 1998; Curio, 2000; Hanajima et al., 2004a; Shima et al., 1991; Hashimoto, 2000). We found that these potentials are widely spread around the volume recorded. In fact, we found VHFOs along trajectories of up to 8 mm and up to 4 mm apart. Obviously, it is difficult to believe that we were inside the V.c. during the entire trajectory. In addition, reconstruction of the trajectory allowed us to identify the nuclei from which VHFOs originated. We also showed that other nuclei not traditionally associated with somatosensory processing, such as the Ce or V.im., show VHFOs during SSEP. Interestingly, the nucleus with a higher probability of showing these potentials was the Ce and not the V.c as expected. These potentials are unequivocally associated with SSEP from the contralateral arm but cannot mark the presence of the V.c. nucleus. Nonetheless, our results indicated that sensory processing includes other thalamic nuclei traditionally ascribed to other functions. Therefore, VHFOs do not serve as a marker for the somatic-sensory relay nucleus of the thalamus.

However, to the best of our knowledge, we characterized a new potential that has not been previously described. We termed these potentials HFOs because their frequency was half that of VHFOs. Nevertheless, frequency as well as the rest of the features were also different. In fact, although HFOs always appeared superimposed onto VHFOs, they were delayed and higher in amplitude. The most relevant is that HFOs are very well located spatially, abruptly appearing in isolated points along trajectories. In contrast to VHFOs and even more significantly, we found HFOs in the V.c. only. Therefore, we propose that these potentials are related to the synapses between lemniscal fibres and thalamo-cortical neurons, although we do not know the sources. This finding is important from a physiological and scientific point of view as well as in thalamic surgery because HFOs appear to be the real landmark of the V.c. and can be evaluated in patients under general anaesthesia, making DBS easier in thalamic surgery and increasing precision in targeting and decreasing the side effects of stimulation.

Finally, importantly, our data were obtained from a small number of patients. Although these data seem to be robust, we need a larger cohort to unequivocally establish these results.

4.1. Conclusions

In this work, we demonstrated that the processing of SSEP at the thalamus in anaesthetized humans includes other nuclei not previously associated with sensory processing because it is associated with the participation of the Ce and V.im. In addition, we described a new thalamic potential that is spatially defined and exclusively present in the V.c nucleus, which is most likely related to the synapses between medial lemniscus and thalamo-cortical relay neurons. From a clinical point of view, the presence of HFOs in patients under general anaesthesia is very important because it can serve as a landmark to positively identify the V.c in thalamic DBS surgery.

Declaration of Competing Interest

None.

Acknowledgements

This work was financed by a grant from the Ministerio de Sanidad FIS PI17/02193 and was partially supported by FEDER (Fonds Europeen de Developpement Economique et Regional). The authors want to acknowledge the collaboration during surgeries by neurosurgeons Marta Navas and Cristina Torres and anaesthesiologists María Luisa Meilán and Eva de Dios.

Authors and contributors

Substantial contributions to conception and design: JP. Acquisition of data: JP and LVZ. Analysis and interpretation of data: JP and LVZ. Drafting the article: JP. Revising the article critically for important intellectual content: LVZ. Final approval of the version to be published: JP.

Appendix A

See Tables A1 and A2.

Table A1
Real coordinates (x_r and y_r) of the macroscopic electrode measured by MRI. Z-coordinate was not used to trajectory reconstruction.

Patient	Right (mm)			Left (mm)		
	x_r	y_r	z	x_r	y_r	z
1	9.6	−8.8	−1.4	7.7	−11.4	−0.5
2	8.4	−10.0	−0.2	8.1	−10.2	−1.5
3	7.6	−9.4	−1.8	7.2	−10.9	1.4
4	7.2	−8.7	1.1	8.6	−8.8	−2.2
5	7.5	−9.6	2.1	7.4	−11.1	−1.7

Table A2
Descriptive statistic for the error between electrode position obtained from reconstructed trajectory and orthogonal projections to SW planes.

SW plane	N	Median	IP25-75	Mean	SEM
Sagittal	480	0.41	0.91	0.72	0.06
Frontal	480	0.98	1.32	1.16	0.07
Axial	480	0.87	0.92	0.91	0.05

Appendix B. Reconstruction of trajectories

If we name the ring angle as α and arch as β, we can obtain any point at distance d from the $\vec{r}_{ep}$ according to these expressions

$$d_1 = \frac{\cos(\beta)d}{\sqrt{\sin(\beta)^2\sin(\alpha)^2 + \cos(\beta)^2}}$$

$$d_2 = \frac{\sin(\alpha)d}{\sqrt{\sin(\beta)^2\sin(\alpha)^2 + \cos(\beta)^2}}$$

where d_1 represents the projection onto the sagittal plane and d_2 onto the frontal plane. Then we obtain the point of the central electrode (in Cartesian coordinates of Leksell system) at distance d, using

$$x = d_2\sin(\beta)$$

$$y = d_1\cos(\alpha)$$

$$z = d_1\sin(\alpha)$$

The rest of electrodes are obtained easily considering that are placed at 2 mm and orthogonal to the line going through (x_{ce}, y_{ce}, z_{ce}) and $\vec{r}_{ep}$.

Appendix C. Measures of synchronization

We have used these measures to determine the relationship between two time series $x(t)$ *and* $y(t)$. The cross-correlation is essentially calculated as:

$$\boldsymbol{C_{xy}}(\boldsymbol{\tau}) = \int_{t_{init}}^{t_{end}} \boldsymbol{x}(\boldsymbol{t})\boldsymbol{y}(\boldsymbol{t}+\boldsymbol{\tau})\boldsymbol{dt}$$

where $\tau = 100,\ 500\ \mu s$ and $t_{init} = 13$ ms *and* $t_{end} = 26$ ms.

These measures not only identify and quantify a relationship between two time signals but also indicate the time point of maximum (or minimum) delay. The other tool for assessing the relationship between two time series was Pearson's correlation coefficient, which is defined as follows:

$$\boldsymbol{\rho_{xy}} = \frac{\int_{t_{init}}^{t_{end}} (x(t)-\mu_x)\left(y(t)-\mu_y\right)dt}{\boldsymbol{\sigma_x\sigma_y}}$$

where $\mu_x$and μ_y are the mean values of both series, and σ_x and σ_y are the standard deviations.

This measure indicates the degree of linear dependence between the two series. However, it does not provide exactly the same information as the correlation measurements based on convolution.

Appendix D. Analysis of action potentials

Data were exported to ASCII files, and analyses were performed off-line with the same bandwidth than HFC (0.5–5 kHz). Action potentials (AP) were identified and grouped according to these properties: maximum and minimum amplitude, maximum and minimum value of the first derivative and duration of depolarizing and repolarizing phases. Using Mahalanobis metric we clustered AP from the same neuron and obtained a mean action potential (mAP) classified as negative or positive according to the maximum amplitude of the absolute values of positive and negative deflections (Vega-Zelaya et al, 2016a).

Appendix E. Supplementary material

Supplementary data to this article can be found online at https://doi.org/10.1016/j.clinph.2019.07.026.

References

Brahimaj B, Kochanski RB, Sani S. Microelectrode accuracy in deep brain stimulation surgery. J Clin Neurosci 2018;50:58–61.

Canedo A, Martinez L, Marino J. Tonic and bursting activity in the cuneate of the chloralose-anethetized cat. Neuroscience 1998;84:603–7.

Chen T, Mirzadeh Z, Chapple KM, Lambert M, Evidente VGH, Moguel-Cobos G, et al. Intraoperative test stimulation versus stereotactic accuracy as a surgical end point: a comparison of essential tremor outcomes after ventral intermediate nucleus deep brain stimulation. J Neurosurg 2018;129:290–8.

Curio G. Linking 600-Hz "spikelike" EEG/MEG wavelets ("sigma-bursts") to cellular substrates: concepts and caveats. J Clin Neurophysiol 2000;17:377–96.

Hanajima R, Chen R, Ashby P, Lozano AM, Hutchison WD, Davis KD, et al. Very fast oscillations evoked by median nerve stimulation in the human thalamus and subthalamic nucleus. J Neurophysiol 2004a;92:3171–82.

Hanajima R, Dostrovsky JO, Lozano AM, Hutchison WD, Davis KD, Chen R, et al. Somatosensory evoked potentials (SEPs) recorded from deep brain stimulation (DBS) electrodes in the thalamus and subthalamic nucleus (STN). Clin Neurophysiol 2004b;115:424–34.

Hashimoto I. High-frequency oscillations of somatosensory evoked potentials and fields. J Clin Neurophysiol 2000;17:309–20.

Hassler R. Anatomy of the thalamus. In: Schaltenbrand G, Bailey P, editors. Introduction to stereotaxis with an atlas of the human brain. Stuttgart: Thieme; 1959. p. 230–90.

Hutchison WD. In: Zvi Israel, Kim J. Burchiel, editors. Microelectrode Recording in Movement disorder surgery. New York: Thieme; 2004.

Katayama Y, Tsubokawa T. Somatosensory evoked potentials from the thalamic sensory relay nucleus (VPL) in humans: correlations with short latency somatosensory evoked potentials recorded at the scalp. Electroencephalogr Clin Neurophysiol 1987;68:187–201.

Kato S, Wang Y, Papuashvili N, Okada YC. Stable synchronized high-frequency signals from the main sensory and spinal nuclei of the pig activated by Abeta fibers of the maxillary nerve innervating the snout. Brain Res 2003;959:1–10.

Klostermann F, Funk T, Vesper J, Siedenberg R, Curio G. Double-pulse stimulation dissociates intrathalamic and cortical high-frequency (>400Hz) SEP components in man. Neuroreport 2000;11:1295–9.

Klostermann F, Gobbele R, Buchner H, Curio G. Intrathalamic non-propagating generators of high-frequency (1000 Hz) somatosensory evoked potential (SEP) bursts recorded subcortically in man. Clin Neurophysiol 2002;113:1001–5.

Møller AR. Anesthesia and Its Constraints in Monitoring Motor and Sensory Systems. In: Møller AR, editor. Intraoperative Neurophysiological Monitoring. New York: Springer; 2011.

Morioka T, Shima F, Kato M, Fukui M. Origin and distribution of thalamic somatosensory evoked potentials in humans. Electroencephalogr Clin Neurophysiol 1989;74:186–93.

Nguyen JP, Nizard J, Keravel Y, Lefaucheur JP. Invasive brain stimulation for the treatment of neuropathic pain. Nat Rev Neurol 2011;7:699–709.

Nieuwenhuys R, Voogd J, van Huijzen C, editors. The Human Central Nervous System. New York: Springer-Verlag, Berlin Heidelberg; 2008.

Obwegeser AA, Uitti RJ, Turk MF, Strongosky AJ, Wharen RE. Thalamic stimulation for the treatment of midline tremors in essential tremor patients. Neurology 2000;54:2342–4.

Ortega GJ, Menendez de la Prida L, Sola RG, Pastor J. Synchronization clusters of interictal activity in the lateral temporal cortex of epileptic patients: intraoperative electrocorticographic analysis. Epilepsia 2008;49:269–80.

Owen SL, Green AL, Stein JF, Aziz TZ. Deep brain stimulation for the alleviation of post-stroke neuropathic pain. Pain 2006;120:202–6.

Pastor J, Hernando-Requejo V, Domínguez-Gadea L, de Llano I, Meilán-Paz ML, Martínez-Chacón JL, et al. Impact of experience on improving the surgical outcome in temporal lobe epilepsy. Rev Neurol 2005;41:709–16.

Peppe A, Gasbarra A, Stefani A, Chiavalon C, Pierantozzi M, Fermi E, et al. Deep brain stimulation of CM/PF of thalamus could be the new elective target for tremor in advanced Parkinson's Disease? Parkinsonism Relat Disord 2008;14:501–4.

Rey HG, Pedreira C, Quian Quiroga R. Past, present and future of spike sorting techniques. Brain Res Bull 2015;119:106–17.

Semenova U, Raeva S, Sedov A. Participation of the thalamic CM-Pf complex in movement performance in patients with dystonia. Mov Disord 2016;31:1398–404.

Shields DC, Cheng ML, Flaherty AW, Gale JT, Eskandar EN. Microelectrode-guided deep brain stimulation for Tourette syndrome: within-subject comparison of different stimulation sites. Stereotact Funct Neurosurg 2008;86:87–91.

Shima F, Morioka T, Tobimatsu S, Kavaklis O, Kato M, Fukui M. Localization of stereotactic targets by microrecordings of thalamic somatosensory evoked potentials. Neurosurgery 1991;28:223–9.

Sloan TB. Anesthesia and motor evoked potential monitoring. In: Deletis V, Shils JH, editors. Neurophysiology in Neurosurgery. Amsterdam: Academic Press; 2002. p. 451–74.

Sola RG, Hernando-Requejo V, Pastor J, García-Navarrete E, DeFelipe J, Alijarde MT, et al. Pharmacoresistant temporal-lobe epilepsy. Exploration with foramen ovale electrodes and surgical outcomes. Rev Neurol 2005;41:4–16.

Usui N, Terada K, Baba K, Matsuda K, Nakamur F, Usui K, et al. Very high frequency oscillations (over 1000 Hz) in human epilepsy. Clin Neurophysiol 2010;121:1825–31.

Valentín A, García Navarrete E, Chelvarajah R, Torres C, Navas M, Vico L, et al. Deep brain stimulation of the centromedian thalamic nucleus for the treatment of generalized and frontal epilepsies. Epilepsia 2013;54:1823–33.

Van Drongelen W. Filters: digital filters. In: Van Drongelen W, editor. Signal Processing for Neuroscientists. Amsterdam: Elsevier; 2007a.

Van Drongelen W. Wavelet analysis. Signal Processing for Neuroscientists. Amsterdam: Elsevier; 2007b.

Vega-Zelaya L, Torres C, Sola RG, Pastor J. Characterization of thalamic nuclei and somatosensory evoked potentials in anesthetized humans. Clin Neurophysiol 2016a;127:e203–5.

Vega-Zelaya L, Garnés-Camarena O, Sánz-García A, Ortega GJ, Pastor J. Mathematical foundations of quantified electroencephalography. Clin Adv Neurophysiol 2016b;10(February).

Vega-Zelaya L, Torres CV, Navas-Garcia M, Sola RG, Pastor J. New thalamic potential associated with somatosensory evoked potentials. Rev Neurol 2017;65:322–6.

Vega-Zelaya L, Pastor J. Intraoperative neurophysiological monitoring techniques for the resection of malignant brain tumors located in eloquent cortical areas. Austin J Neurosurg 2015;2:1038.

Vega-Zelaya L, Sola RG, Pastor J. Intraoperative neurophysiological monitoring in neuro-oncology. In: Agarwal A, editor. Neurooncology. InTech; 2016c. p. 207–49. ISBN 978-953-51-2425-2.

Voss LJ, Sleigh JW, Barnard JP, Kirsch HE. The howling cortex: seizures and general anesthetic drugs. Anesth Analg 2008;107:1689–703.

Wu D, Wang S, Stein JF, Aziz TZ, Green AL. Reciprocal interactions between the human thalamus and periaqueductal gray may be important for pain perception. Exp Brain Res 2014;232:527–34.

Yamashiro K, Tasker RR, Iwayama K, Mori K, Albe-Fessard D, Dostrovsky JO, et al. Evoked potentials from the human thalamus: correlation with microstimulation and single unit recording. Stereotact Funct Neurosurg 1989;52:127–35.

Yeh IJ, Tsang EW, Hamani C, Moro E, Mazzella F, Poon YY, et al. Somatosensory evoked potentials recorded from the human pedunculopontine nucleus region. Mov Disord 2010;25:2076–83.